

Ionospheric effect on the synthetic Epoch of Reionization observations with the SKA1-Low

Samit Kumar Pal,^{a,1} Abhirup Datta,^a Aishrila Mazumder^{b,a}

^aDepartment of Astronomy, Astrophysics & Space Engineering, Indian Institute of Technology Indore, Indore 453552, India

^bJodrell Bank Centre for Astrophysics, Department of Physics and Astronomy, The University of Manchester, Manchester M13 9PL, UK

E-mail: palsamitkumar@gmail.com

Abstract. The redshifted 21 cm signal of neutral hydrogen can be used as a direct probe of the intergalactic medium during Cosmic Dawn (CD) and Epoch of Reionization (EoR). However, detecting this inherently weak signal has numerous challenges. The major ones include accurate foreground removal from low-frequency radio observations and systematics arising from instrumental effects. The Earth’s ionosphere poses a major obstacle at these low radio frequencies. Thus, a systematic study of ionospheric effects on these sensitive low-frequency observations is critical, given that the construction of the Square Kilometre Array (SKA1-Low) is in full progress. We use the end-to-end pipeline, called 21CME2E, to study the effect of time-varying ionospheric corruption on the 21 cm power spectrum recovery. We use two models: a) a catalogue-based model focused on source position shift due to the refractive effect of the ionosphere and b) a realistic ionospheric condition generated using Kolmogorov’s turbulence model. We assess the effect of the imperfections thus generated on the extraction of H_I 21 cm signal power spectrum. Our study shows that beyond “median ionospheric offset” ($\theta_{\text{MIO}} \lesssim 0.1''$), the 21 cm signal from the EoR is unaffected by residual ionospheric effects. Our study emphasizes the need for the development of efficient ionospheric calibration algorithms for the upcoming SKA1-Low observations to extract the H_I 21 cm power spectra from the CD/EoR.

Keywords: Statistical sampling techniques, power spectrum, reionization, cosmological simulations

¹Corresponding author.

Contents

1	Introduction	1
2	Simulations	3
2.1	EoR model	4
2.2	Foreground model	5
2.3	Telescope model	5
2.4	Ionospheric models	6
2.4.1	Case I	7
2.4.2	Case II	8
2.5	Synthetic observations	9
3	Ionospheric effect on imaging	10
3.1	Offsets distribution	10
3.2	Analysis method	12
3.3	Tolerances	13
3.3.1	Case I	13
3.3.2	Case II	13
4	PS estimation	15
4.1	Analysis method	15
4.2	Systematics effect on PS estimation	16
4.2.1	Case I	16
4.2.2	Case II	17
5	Summary and conclusions	18

1 Introduction

One of the main aims of the upcoming Square Kilometer Array (SKA1-Low) radio interferometer is to observe the Cosmic Dawn (CD) and Epoch of Reionization (EoR) era. The CD/EoR is a critical period for the structure formation in the early universe. It marks the transition from neutral hydrogen (HI) dominated intergalactic medium (IGM) to an ionized one. It occurred when ultraviolet (UV) radiation of the first luminous objects, such as the first stars and galaxies, started stripping electrons from these abundant HI atoms. Many complementary probes used hydrogen, the most abundant baryonic element in the early universe, to study these epochs. Observations of the cosmic microwave background (CMB) and its interaction with free electrons (Thompson scattering [1]) constrain the reionization history [2]. Additionally, studies of the luminosity function and clustering properties of Ly α emitters [3, 4] and high-redshift quasars emitting Ly α radiation [5–7] provide further insights. This combined evidence suggests that reionization is nearing completion at a redshift of $z \sim 6$ [2]. The HI 21 cm line, originates when an electron in the ground state undergoes a spin flip

from a parallel to an antiparallel state. This helps us trace the entire reionization history and thus will answer many questions related to EoR science [8–10].

In the past decade, radio interferometers like the Murchison Widefield Array [MWA, 11–13], the LOw Frequency ARray [LOFAR, 14]), Giant Meterwave Radio Telescope [GMRT, 15], Precision Array to Probe Epoch of Reionization [PAPER, 16] and Hydrogen Epoch of Reionisation Array [HERA, 17–19] focused on detecting these signal from the early epoch of the universe. While the H_I 21 cm signal is the desired observable, it is not the only emission detected. Astrophysical foreground emission, like galactic synchrotron radiation and extragalactic free-free emission, also contributes to the overall measured signal. The desired EoR signal exhibits statistical isotropy and a fluctuating spectrum, whereas the foreground signals exhibit a spectrally smooth spectrum and are thereby structureless. In Fourier space, the spectrally smooth foreground emission is confined to the wedge-shaped region and is localized by the horizon line. A wedge is a definite result of the chromaticity of the instrument. The region expected to be free from foreground contamination in Fourier space is known as the EoR window. Therefore, for extracting the H_I 21 cm signal, the wedge-shape structure is avoided. This approach is known as the foreground avoidance technique [20–23]. Another method involves subtracting the foreground using either a parametric or non-parametric model, known as the foreground removal technique [24–26]. Precise instrument calibration is essential for accurate foreground modeling and subtraction [27–34]. There are other contaminations, for example the instrument model [35–38], incomplete sky model [28], and PS estimation [28, 39–44] Earth’s ionosphere [45–47], radio frequency interference (RFI) [48], and instrumental primary beam [49, 50].

In the past decade, extensive study have been carried out on understanding and quantifying these residual contaminations. The Earth’s ionosphere, coupled with a bright foreground, plays a major role in the systematic effects. Ionospheric refraction shifts the incident radio waves from the cosmic sources, thereby leading to changes in their positions in the image plane. It occurs due to transverse variation of the density of electrons (total electron content, i.e., TEC) column along the line-of-sight, aligning with the direction of the gradient. This effect varies with change in direction [51]. The relationship between the $\vec{\nabla}\text{TEC}$ and the resulting angular offset $\delta\vec{\theta}$ is described by Equation 1.1:

$$\vec{\nabla}\text{TEC} = 1.20 \times 10^{-4} \left(\frac{\nu}{100 \text{ MHz}} \right)^2 \left(\frac{\delta\vec{\theta}}{1''} \right) \text{TECU km}^{-1} \quad (1.1)$$

This effect primarily depends on the observing frequency (which, in our case, dominates other effects) and the spatial distribution of the TEC in the ionosphere. During the PS estimation, MWA excludes the data observed in the duration of high ionospheric activity [12, 46, 52]. Since SKA1-Low will be housed at the Murchison Radio-astronomy Observatory (MRO) site in Western Australia, it will face the same ionospheric conditions on the EoR observations. The ionosphere causes deviation from the true sky, resulting in the inaccurate removal of compact extra-galactic sources and creating large residuals in the dataset. This residual gets propagated into PS, resulting in a bias estimation of 21 cm PS.

Beardsley et al. [53] reported the upper limit of EoR PS at redshifts between 6.5 and 7.5 using MWA EoR experiments. They observed that at small k -values, the data was dominated by systematics. The foreground contamination contributed to excess power because significant

ionospheric activity caused calibration errors. In another recent study, the authors [13, 19] reported the upper limit of the HI 21 cm signal power amplitude from the MWA-II telescope and HERA phase-II telescope. The author [54] reported the upper limit of the X-ray heating epoch based on two nights of different ionospheric activity constrained by calibration systematics. Gan et al. [55] assessed the impact of different direction-dependent calibration methods on the LOFAR 21 cm signal power spectrum (PS) during NCP observations. Thus, it can be concluded that systematic effects primarily constrain the upper limits. In this study, we revisited the problem of ionospheric contamination in the k -modes and showed how nuisance ionospheric contamination affects realistic EoR observations.

Here, we have used the end-to-end pipeline, 21CME2E that has been outlined in [34]. We have used a 21 cm signal model and T-RECS catalogue as a model sky and introduced two different ionospheric models as the corrupting term in the simulations. Our goal is to understand the effect of ionospheric contamination on the synthetic EoR observations using the compact core of SKA1-Low with a maximum baseline of 2 km (2). Our analysis examines when ionospheric interference starts hindering the detection of the HI 21 cm signal. It highlights how ionospheric effects mainly affect foreground-dominated k modes, leading to residual contamination that obscures the target signal within the EoR window. In addition, we investigated how ionospheric corruption affects the dynamic range of the images in the detection of the desired EoR signal. A similar analysis was performed by [34] using a radio interferometer at low frequencies ($z \sim 9$), addressing the antenna-based gain calibration error and position error with synthetic observations.

This paper is organized as follows: Section 2 details the setup of our simulation framework for synthetic SKA1-Low observations. Section 3 discuss the impact of ionospheric corruption on extracting the HI signal from the image plane for different scenarios. Section 4 presents the results of PS estimation and the conclusions drawn for EoR. Finally, Section 5 summarizes our key findings from our analysis. The best-fitted cosmological parameters from the Planck 2018 results [2] were used throughout this study, with the following details: $\Omega_M = 0.31$, $\Omega_\Lambda = 0.68$, $\sigma_8 = 0.811$, $H_0 = 67.36 \text{ km s}^{-1} \text{ Mpc}^{-1}$.

2 Simulations

This section focuses on generating synthetic observations using ionospheric models. Figure 1 shows a schematic block diagram of the 21CME2E¹ pipeline. The observation parameters are listed in Table 1. The following subsections briefly describe each parameter in the input block. The simulations have been performed on the OSKAR² software, and Common Astronomy Software Application (CASA³ [56]) was used to construct the image from visibility data. OSKAR uses the radio interferometer measurement equation [57] to generate full stroke visibility data. In this work, a four-hour observation period (± 2 HA) tracks the sky with the phase centre pointed at $\alpha = 15h00m00s$ and $\delta = -30^\circ 00m00s$ using a 120 second

¹<https://gitlab.com/samit-pal/21cme2e.git>

²<https://github.com/OxfordSKA/OSKAR/releases>

³https://casaguides.nrao.edu/index.php?title=Main_Page

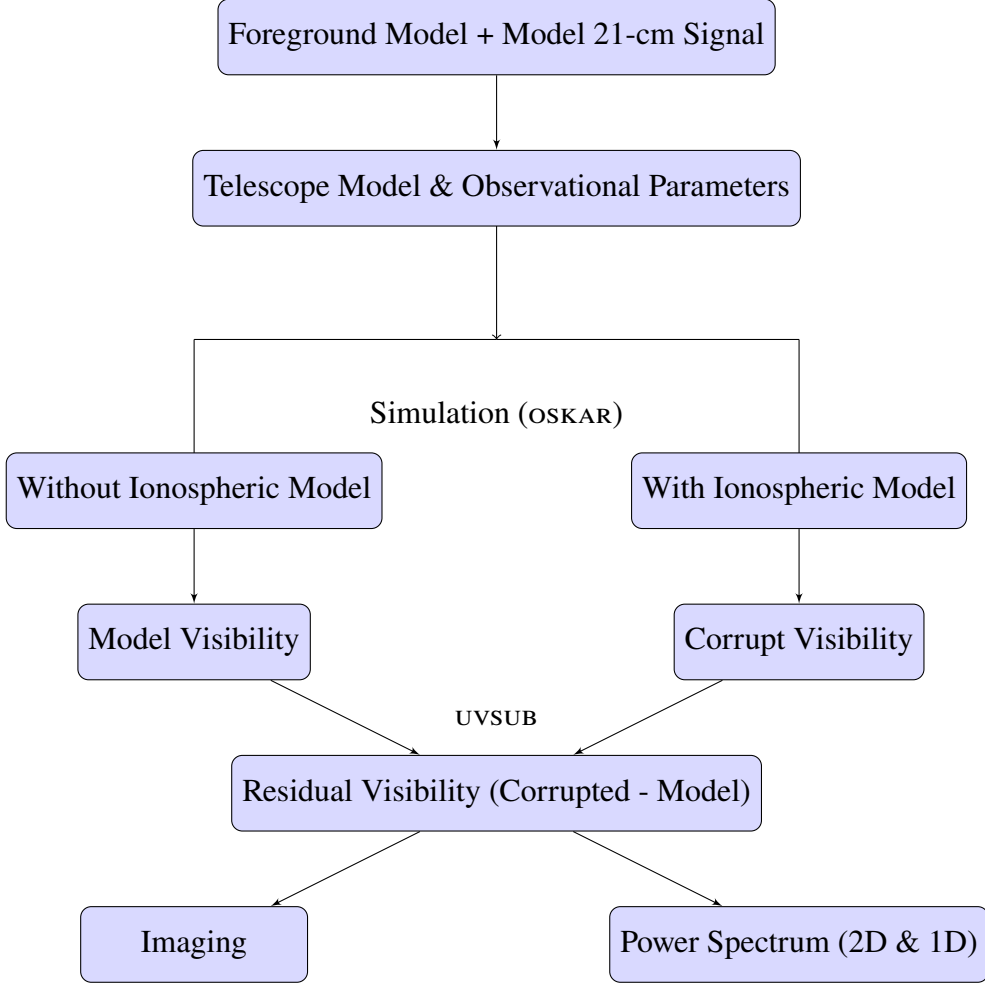


Figure 1: Schematic diagram of the 21CME2E pipeline.

integration time and bandwidth of 8 MHz at a centre frequency of 142 MHz ($z \sim 9$) with a channel separation of 125 kHz (64 channels).

2.1 EoR model

The differential brightness temperature (δT_b) of the H_I 21 cm signal during EoR, can be expressed as:

$$\delta T_b \approx 27 x_{\text{HI}} (1 + \delta) \left(\frac{1+z}{10} \right)^{\frac{1}{2}} \left(1 - \frac{T_{\text{CMB}}(z)}{T_S} \right) \left(\frac{\Omega_b}{0.044} \frac{h}{0.7} \right) \left(\frac{\Omega_m}{0.27} \right)^{-\frac{1}{2}} \text{ mK} \quad (2.1)$$

where x_{HI} is the neutral fraction of hydrogen, δ is the density fluctuation, H is the evolving Hubble constant, $T_{\text{CMB}}(z)$ is the CMB temperature at a redshift of z and T_S is the spin temperature of the two states of hydrogen [8]. We use a simulated H_I 21 cm fiducial lightcone cube generated from the semi-numerical simulation, 21CMFAST [58, 59]. For our analysis, we used the existing simulated H_I 21 cm maps from Mazumder et al.[34]. The simulated light cone covers a comoving sky-plane area of $500 \times 500 h^{-1} \text{Mpc}^2$, a redshift range of

Table 1: An overview of the observational parameters used in the simulations.

Parameter	Value
Central frequency	142 MHz ($z \sim 9$)
Bandwidth	8 MHz
Spectral Resolution	125 kHz
Field of view (FoV)	4°
Number of array elements(N_a)	296
Maximum baseline	~ 2000 m
Synthesized beam	$\sim 2.5'$
Polarization	Stokes I
No. of snapshots	120
Integration time per snapshot	2 minutes
Phase Center(J2000)	RA, DEC= 5 h, -30°
Effective collective area (A_{eff})	962 m^2
Core area of an array (A_{core})	12.57 km^2
Total collecting area of the array (A_{col})	$N_a A_{\text{eff}}$

$7.0 \leq z \leq 12.0$ and has a grid size of $232 \times 232 \times 562$. A specific cuboid region of size $232 \times 232 \times 64$ was extracted for analysis. This cuboid was then converted from comoving Mpc to angular-frequency (WCS) coordinate for the input of the 21cME2E pipeline.

2.2 Foreground model

A sky model with high resolution in both angular and frequency space is essential to precisely estimate the foregrounds observable by SKA-Low. Following the methodology outlined in [34], we employ the point source foreground model from the Tiered Radio Extragalactic Continuum Simulation (T-RECS) [60]. This model uses a flux range of 0.6 Jy to 3.1 mJy at 150 MHz. Fluxes were then converted to their corresponding values at 142 MHz using a spectral index (α) of -0.8 , which follows the power law relationship, $S_\nu \propto \nu^{-\alpha}$. For this study, we excluded the diffuse foreground model and focused solely on point sources only. Readers can refer to [34] for a detailed description of the foreground model.

2.3 Telescope model

The highly sensitive next-generation telescope SKA1 will make tomographic maps of the H_I 21 cm signal and also precision signal PS measurements. The SKA will consist of two separate arrays: a low-frequency array in Western Australia operating between 50–350, MHz, and a mid-frequency array in South Africa operating between 350, MHz and 14, GHz. CD/EoR observations are done at frequencies $\lesssim 200$ MHz, and will thus use the SKA1-Low. SKA1-Low is being built at the Murchison Radio-astronomy Observatory (MRO) site in Western Australia, where the MWA is currently located. The initial configuration of the SKA1-Low

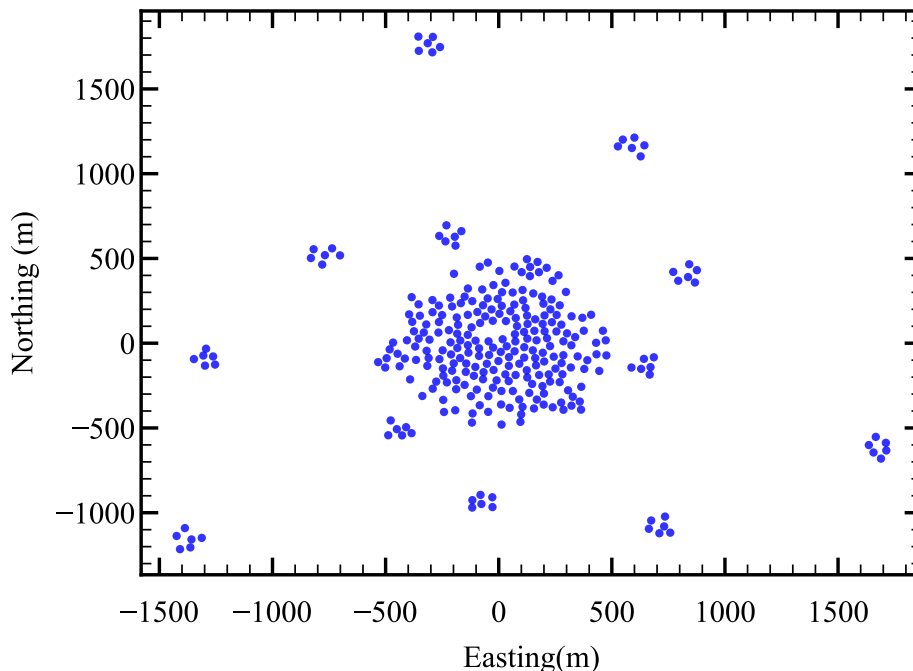


Figure 2: The SKA1-Low telescope layout for 296 stations with a maximum baseline of 2 km around the central core.

will have 512 stations of 40 m diameter, each with 256 dipole antennas, dispersed in a dense core and spiral arms with a maximum baseline length of ~ 70 km [61]. The impact of different ionospheric conditions on SKA1-Low will be similar to that of the MWA telescope. This study focuses on the compact core with a maximum baseline distance of 2 km from the centre station. The compact configuration of the baseline is crucial for EoR observations as the H_I 21 cm signal presents itself as a diffuse background with its predominant power concentrated on large angular scales or small k -scales. Consequently, shorter baselines mostly contribute to the sensitivity of the instrument to the H_I signal from EoR. The expected telescope configuration of the SKA1-Low is illustrated in Figure 2. A detailed study of the ionospheric effect on the longer baselines and other systematics is beyond the scope of this work and will be the subject of a future study.

2.4 Ionospheric models

This work aims to demonstrate how ionospheric effects translate to foreground leakage on the residual visibilities used in final power spectrum estimation. Ionospheric refraction causes an apparent shift of point sources from their original position. We investigate how different levels of ionospheric activity, ranging from extremely active to quiet, affect k -modes (spatial scale) in cosmological PS. To quantify the impact of ionospheric contamination on PS estimation. We present two approaches for simulating ionospheric effects. The first method leverages a catalogue-based model to introduce refraction shifts in point sources based on the previous MWA observations. The second approach employs Kolmogorov’s turbulence model to create a more realistic representation of ionospheric conditions reflecting the ambient ionospheric

activity at the MRO location. We will describe each of these models in detail in the following subsections. The refractive shift and Kolmogorov’s turbulence model are referred to as Cases I and II, respectively. Using these frameworks, we can assess how ionospheric contamination manifests itself within CD/EoR science, separating it from other observational effects.

2.4.1 Case I

The inhomogeneity in density of the plasma of the ionosphere introduces additional phase shifts in electromagnetic waves that vary with time, frequency, and position. In radio interferometry, these phase shifts manifest as apparent shifts in the position of the source in the image plane. To accurately simulate the effect of the ionosphere, we need knowledge about ionospheric conditions at the location of the SKA1-Low telescope. This telescope is being constructed at the MRO site, where the MWA currently operates as a precursor to SKA1-Low. According to the Fourier shift theorem, a position shift in the image plane corresponds to a phase shift in the Fourier domain (i.e., u-v domain). We used a Gaussian distribution to simulate shifts in apparent source positions. This mimics the effects of refraction shifts caused by turbulent plasma in the ionosphere. These shifts affect the phase of radio waves in synthetic SKA1-Low observations.

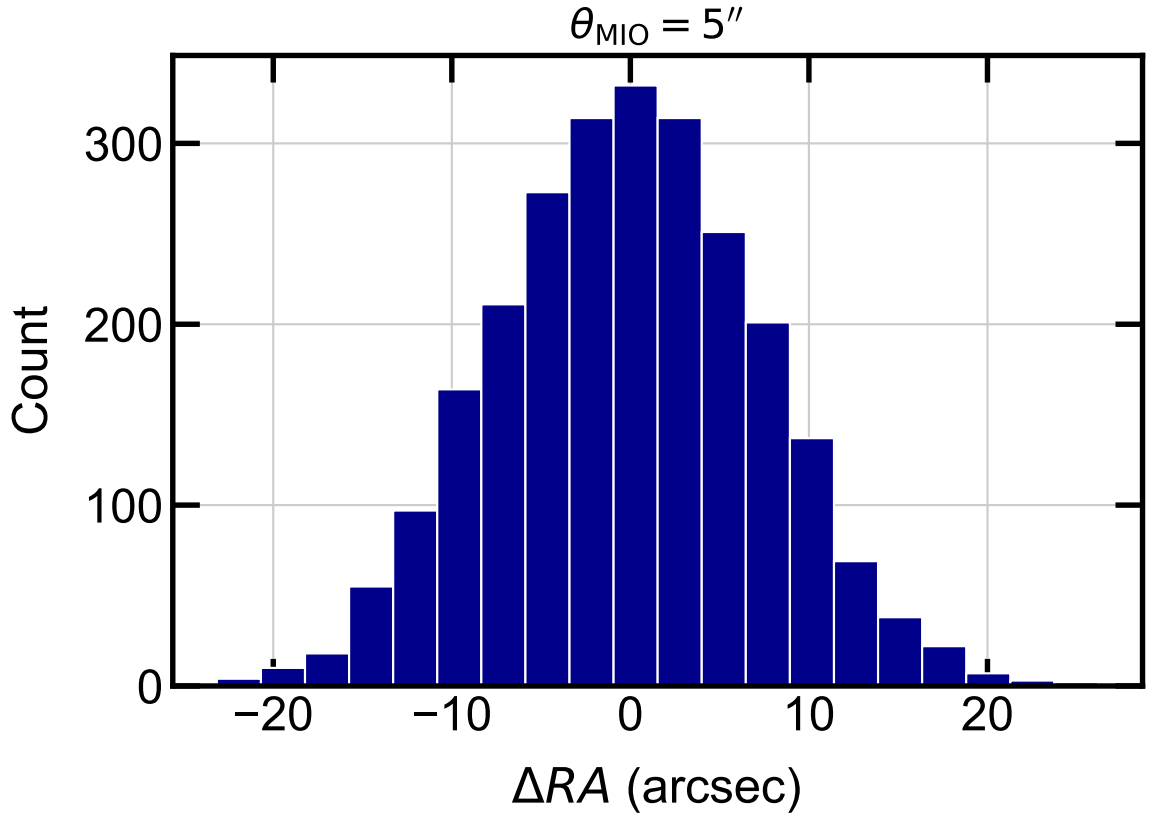


Figure 3: Distribution of angular shifts in the sources of the catalogue with $\theta_{\text{MIO}} = 5.0''$, simulated at 142 MHz for a single snapshot.

Previous MWA-based research by Jordan et al.[45] characterized the ionospheric activity in the MRO based on the position offset of known sources within the field of view of observations. Such position offsets are then characterized by the metric median ionospheric offset (MIO). Furthermore, Jordan et al. [45] defined quiet ionospheric conditions for the MWA EoR experiment based on a threshold for MIO of $0.15'$ at 200 MHz. For this study, we have adapted this MIO-based model for the ionosphere. We have used drawn ionospheric offset distributions for different MIOs corresponding to ionospheric activities ranging between active and quiet conditions. In order to simulate the effect of ionospheric phase shift, we added the apparent position shift to each source's right ascension (RA) in the T-RECS [60] catalogue following the above MIO-based offset distribution. These offsets vary for each source across the plane of the sky, capturing the direction-dependent effect due to the ionosphere.

We have modelled a dynamic ionosphere, updated every 2 minutes. This cadence aligns with the time averaging used in the GaLactic and Extragalactic All-Sky MWA (GLEAM) Survey [62]. Furthermore, we have modeled the temporal evolution of the ionosphere as a sinusoidal wave with a period of 4 hours. This results in a temporal evolution of the source offsets against a minor travelling ionospheric disturbance (TID). A histogram of the distribution of angular shifts (RA shifts) in the sources of the T-RECS catalogue with $\theta_{\text{MIO}} = 5''$ for one such snapshot is shown in Figure 3.

2.4.2 Case II

In the previous section, the dynamic ionosphere is modelled in terms of a single TID. However, in reality, the ionosphere is a far more complex 3D structure that evolves in time in all directions. Hence, in this model, we incorporate a thin, two-dimensional phase screen [63] as the ionospheric model. We have used a phase screen that changes in time using Kolmogorov's turbulence model [46, 64, 65]. Mevius et al. [65] reported the value of the spectral index is $\alpha = 3.89 \pm 0.1$ at the LOFAR site. However, for our simulations, we used the pure Kolmogorov turbulence value of $\alpha = 11/3$. The power spectrum of the spatial phase function is given by,

$$\left| \Phi(\vec{k}) \right|^2 \propto \left[k^2 + \left(\frac{1}{L_0} \right)^2 \right]^{-\alpha/2} \exp\left(-\frac{k^2}{2/l_0^2} \right); 1/L_0 \ll k \ll 1/l_0 \quad (2.2)$$

where l_0 and L_0 are the inner and outer scales of the turbulence, respectively, and \vec{k} is the spatial frequency. To account for the time-evolving phase screens, we added a linear function of the phase of the complex spectrum in the Fourier domain. Then the phase function, $\Phi_{\text{new}}(\vec{k})$ becomes [see, for more details 66]

$$\Phi_{\text{new}}(\vec{k}) = \Phi_{\text{old}}(\vec{k}) \exp\left(2\pi i \vec{k} N_s / N \right) \quad (2.3)$$

where N_s is the number of pixels in which the phase screen needs to move in the direction of coordinate \vec{k} and N^2 is the size of the ionospheric layer.

An understanding of the ionospheric structure is crucial for setting the size of turbulent

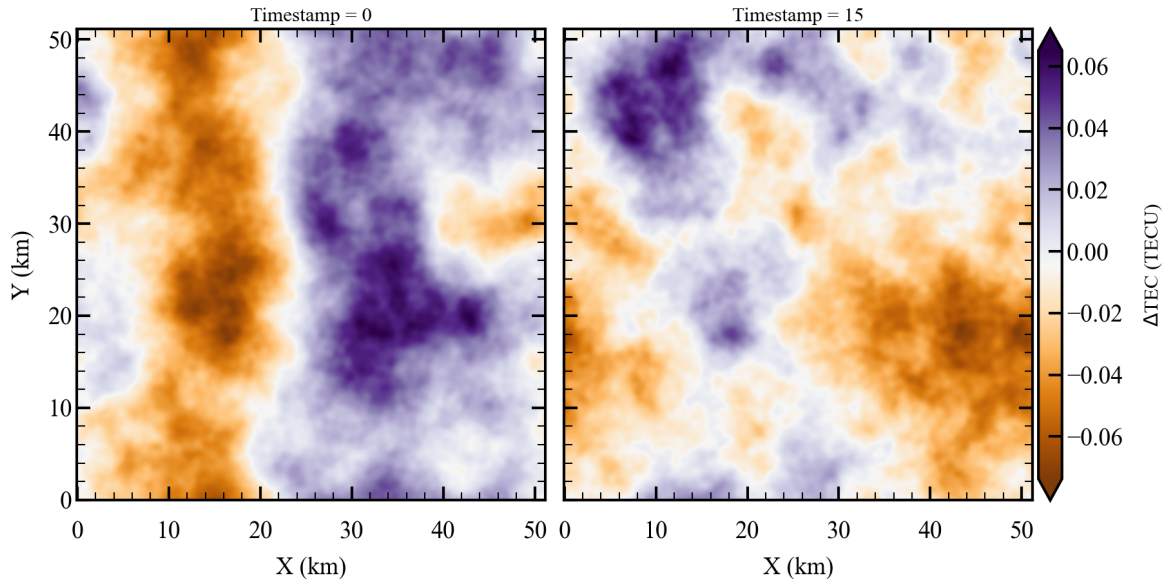


Figure 4: Two slices of a simulated Kolmogorov’s turbulence TEC screen were generated using the FFT algorithm with dimensions $51 \text{ km} \times 51 \text{ km}$ with $\theta_{\text{MIO}} = 5.0''$. At the 400 km altitude, this ionospheric screen covered the sources outside the primary FoV.

elements in general models. However, a comprehensive investigation of the finite scale at the MRO site is beyond the scope of this study. Ionospheric irregularities often occur at the equator and high latitudes, whereas mid-latitude locations such as SKA1-Low experience lower activity levels [67]. GLEAM observations show that the angular scales of the ionospheric structure are typical 100 s of km in the MRO [47]. Therefore, we chose an outer scale size of 100 km for our simulations, consistent with the general estimate provided by GLEAM observations. The SKA1-Low telescope has a field of view (FoV) of $\sim 4^\circ$, and we assume the ionosphere is located at an altitude of 400 km [45] above the Earth’s atmosphere. This altitude corresponds to a projected ionospheric layer with dimensions of 30 km on each side to model the spatial variations of TEC within the field of view. For this study, we simulated a larger ionospheric region of $51 \times 51 \text{ km}^2$. We used a travelling ionospheric disturbance (TID) speed of 75 km/s aligned with the wave vector directions to simulate the turbulent and transient motion of the TID. The dynamic ionosphere, updated every 2 minutes on the telescope-projected beam, which is consistent with Case I. Figure 4 shows two slices of a simulated TEC screen at different timestamps.

2.5 Synthetic observations

The visibility, which encodes the spatial coherence information of the radio sky, is mathematically described by the equation:

$$V(\mathbf{u}, \nu) = \int_{\text{sky}} A(\hat{\mathbf{s}}, \nu) I(\hat{\mathbf{s}}, \nu) e^{-2i\pi(\phi + \phi')} d\Omega \quad (2.4)$$

where \mathbf{u} is the baseline vector, $I(\hat{\mathbf{s}}, \nu)$ & $A(\hat{\mathbf{s}}, \nu)$ is the specific intensity, and the antenna beam pattern, both of which are functions of frequency ν . The additional phase shift ϕ'

accounts for the source-position offset in the image domain. The components of the unit vector $\hat{s}(l, m, n)$ are the direction cosines towards the east, north & zenith, respectively, with $n = \sqrt{1 - l^2 - m^2}$ and $d\Omega = dl dm / \sqrt{1 - l^2 - m^2}$. In this work, primary beam correction is not considered, i.e., $A(\nu)$ is set to 1.

We simulate a model sky with no corruption, which is the true or model sky (V_{ij}^{model}). Then we use the inaccurate sky models to determine the effect of the ionospheric phase shift. Utilizing the aforementioned ionospheric frameworks 2.4, we generated contaminated visibilities, denoted as V_{ij}^{corrupt} . Simulations are done using the settings described in section 2. In both cases, we generated multiple sets of apparent sky models with MIO values of 0.1'', 0.2'', 1'', 5'', and 30''. These MIO values represent the level of ionospheric activity ranging from highly active ($\theta_{\text{MIO}} = 30''$) to extremely quiet ($\theta_{\text{MIO}} = 0.1''$) conditions. These activity levels are comparable to those observed in real MWA data by Jordan et al. [45]. For Case I, we added simulated offset distributions with the corresponding MIO values to the true source positions in RA. In Case II, we scaled the turbulence levels to match the specified MIOs. This scaling represents the simulated ionospheric differential TEC. These turbulence levels, represented by phase screens, introduced an additional phase factor for each source and station within the OSKAR simulations. For detailed information on the simulation of ionospheric contamination, refer to Appendix 5.

Now to remove point sources from the data, we subtracted the true sky model from both sets of simulated ionospheric contaminated sky models in the visibility domain. This subtraction results in the residual visibility, expressed as:

$$V_{ij}^{\text{residual}} = V_{ij}^{\text{corrupt}} - V_{ij}^{\text{model}} \quad (2.5)$$

The observed visibility is denoted by V_{ij}^{corrupt} (the label ‘‘corrupt’’ denotes the actual observations obtained from the ionospheric effect), and V_{ij}^{model} is the true visibility. We utilize the residual visibility, as employed in our previous study [34], to assess the impact on image plane performance and PS estimation. Thermal noise was not considered in this simulation. In the following sections, will discuss the formalism used for image plane effect and PS estimation.

3 Ionospheric effect on imaging

In this section, we present the impact of ionospheric refraction on the extraction of H_I 21 cm signal in the image plane. In addition, we analyze the distribution of the position offsets after propagation through the refractive medium of the ionosphere.

3.1 Offsets distribution

We have investigated how the ionospheric offsets on the position of sources vary due to the ionospheric refractive medium. In order to quantify the offset distribution, we simulated sky models with and without ionospheric effects. The simulated sky is imaged using CASA, using Briggs weighting with robust parameter set to -1 . We extract sources from our simulated sky images using AEGERAN⁴ [68] source finder tool. Catalogues thus generated from AEGERAN

⁴<https://github.com/PaulHancock/Aegean>

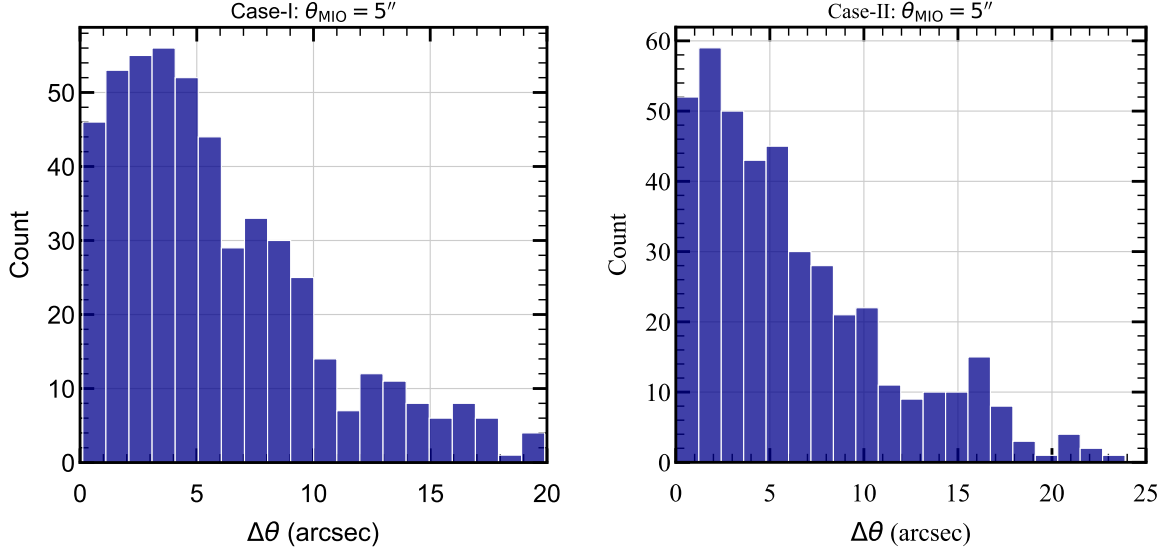


Figure 5: Histogram of the distribution of offsets of selected point sources with MIO of $5''$ for (left) position shift due to refraction (Case I) and (right) Kolmogorov turbulence (Case II). These offsets are measured relative to the time-averaged positions of the sources. Case II has more offset outliers than Case I. This significant difference in outlier behaviour translates to vastly different sky models, affecting the subtraction of foreground models and varying tolerance levels in the extraction of the H α signal.

have angular positions, integrated flux densities and their associated errors, which are used for studying the impact in the image domain. We select compact sources having high SNR, i.e. flux densities greater than 5 times the RMS noise in that image (5σ). The offset for each coordinate has been set as:

$$\Delta\alpha = \alpha_{\text{ionosphere off}} - \alpha_{\text{ionosphere on}} \quad (3.1)$$

$$\Delta\delta = \delta_{\text{ionosphere off}} - \delta_{\text{ionosphere on}} \quad (3.2)$$

The position offset due to the ionosphere is calculated as:

$$\Delta\theta = \sqrt{(\Delta\alpha)^2 + (\Delta\delta)^2} \quad (3.3)$$

Figure 5 shows the histogram of the offset distribution of the selected point sources for both cases with the MIO of $5.0''$. These offsets are measured relative to the time-averaged positions of the sources. The median ionospheric offset (θ_{MIO}) of these histograms serves as a metric for quantifying the level of ionospheric activity. This metric signifies the amplitude of the TEC gradient of the ionosphere. Case II exhibits a larger offset outlier compared to Case I at the equivalent MIO value. This significant difference in outlier behaviour translates to vastly different sky models, affecting the subtraction of foreground models. Incomplete foreground removal degrades the dynamic range of the EoR signal, further hindering its

detection. The severity of these effects correlates with source SNR. Lower SNR sources experience a larger apparent offset due to the ionosphere, leading to a significantly different sky model than high SNR sources. Therefore, this unique contamination in each case poses a significant challenge for extracting the target signal in both PS and image domains.

3.2 Analysis method

One of the key science projects for SKA1-Low is to make the tomographic images of the H_I 21 cm signal with a SNR $\gtrsim 1$ [69] at scales from several arcminutes to several degrees. One can use various image-based statistical tools, such as the Minkowski functional [70] and the Largest Cluster statistic [71, 72], to extract maximum information from the signal. However, it is essential to understand how ionospheric errors affect the image plane detection of the 21cm signal. Ionospheric errors can result in imperfect source removal and affect the accuracy of calibration and imaging. Therefore, it is crucial to investigate and mitigate such errors.

As expected, the instant sky deviates from the true sky emission and creates imperfect subtraction, i.e. the residuals may contain a significant amount of foreground emission. One of the major aims of this study is to investigate the threshold at which the target signal becomes obscured by ionospheric disruptions. The effect of Earth’s ionosphere significantly limits the dynamic range. Ionospheric noise affects the visibility phases and adds additional effective noise to residual images. This error limits the achievable dynamic range, regardless of the source flux density. The RMS noise increases as the position of the source increases from the phase centred in the residual image. The RMS noise characteristic can change depending on what kind of gridding scheme is used. In order to estimate the RMS noise from the residual visibility, we generated a dirty image using `CASA tclean` task using the natural weighting scheme. The RMS noise limit was then estimated within a region near the phase centre of this image. We use RMS noise against the MIO as a quantifying metric in the image plane to analyse the detectability of the H_I 21 cm signal. However, to achieve detection of the H_I 21 cm signal, the RMS should be below the signal level. The signal at 142 MHz has a peak flux of $\sim 0.8 \mu\text{Jy beam}^{-1}$. Thus, for a residual value beyond this, the target signal becomes obscured. We also measured the dynamic range (DR) to assess image plane performance. The dynamic range is the ratio of the highest peak flux and the RMS noise in an unsourced region in the image. Perley et al. [73] calculated an equation for DR for N antennas for M independent successive snapshots and is given by,

$$\text{DR} = \frac{\sqrt{MN}}{\phi_0} \quad (3.4)$$

where ϕ_0 is the time-independent phase error (in radians) for all the baselines.

In order to detect the faint EoR signal, we must suppress the thermal noise level of the instrument, which reflects the sensitivity of the instrument. The thermal noise of the instrument is estimated from the radiometer equation:

$$\sigma_N = \left(\frac{2k_B}{A_{\text{eff}}N_{\text{ant}}} \right) \left(\frac{T_{\text{sys}}}{\sqrt{n_p \Delta\nu t_{\text{int}}}} \right) \quad (3.5)$$

where σ_N denotes the thermal noise of the instrument, $\Delta\nu$ denotes the channel width, t_{int} denotes the integration time, T_{sys} denotes the system temperature, A_{eff} denotes the effective area of each station, n_p denotes the number of polarization, and the N_{ant} denotes the number of antennas. The sky temperature T_{sky} is the same as the system temperature T_{sys} of the instrument at this frequency because we assume that our simulation is free from noise. The sky temperature $T_{\text{sky}} = 180 (\nu/180 \text{ MHz})^{-2.6} \text{ K}$ [8]. According to the 3.5 equation, the thermal noise is $\sim 4.8 \mu\text{Jy}/\text{beam}$ after 1000 hours of integration time with a channel width of 125 kHz, an effective area of 962 m² and a system temperature of 333 K. This scenario is shown in Figure 6 by the magenta dashed line for an optimistic scenario. However, thermal noise was not included in our simulations to isolate the ionospheric effects.

3.3 Tolerances

To quantify the threshold at which ionospheric contamination hinders the detection of the H_I 21 cm signal, we studied the variation in the RMS noise with the MIOs. This variation of RMS noise is observed over a 4 hour observation period for different ionospheric frameworks. The comparison of RMS noise variation against MIO of these ionospheric frameworks is shown in Figure 6 (as discussed in Section 3.2). The following subsections describe the different cases used in the analysis.

3.3.1 Case I

The dash-dotted blue line shows the effect of the ionospheric error on SKA1-Low in the image plane in Figure 6 for Case I (refractive shift). It is observed that at the MIO value of 0.1'', the RMS noise falls within the error bars and overlaps with the signal level (represented by the grey band). This optimistic scenario clearly detects the H_I 21 cm signal, assuming the observed sky solely comprises this signal. However, beyond this MIO, the RMS noise surpasses the signal level, potentially hindering or obscuring its detection. This highlights that for a sufficient integration time, systematic errors introduced by the ionosphere become more critical than random thermal noise in limiting the observations. In addition, this effect effectively reduces the dynamic range (DR) of the residual image. The observed DR for this scenario is $\sim 10^5$.

3.3.2 Case II

The dotted red line in Figure 6 represents the effect of the ionospheric error on SKA1-Low in the image plane for Case II (Kolmogorov turbulence model). Similarly, at the MIO value of 0.2'', the RMS noise within the error bar falls in between the target signal level and enables target signal detection. The theoretical value of DR is estimated to be $\sim 10^5$, based on Equation 3.4. We achieve a DR of approximately 10^5 from a dirty image. However, the required dynamic range for the EoR signal detection is approximately 10^8 [74]. Therefore, an optimum astrometric accuracy of 0.2'' is crucial for extracting the H_I 21 cm signal from the image plane.

Figure 6 also shows the thermal noise limit for 4 hours of observation time. A typical limit of observing time per day is about ± 2 hours around the transit time of the source field. If we assume that there are no systematics left over from the analysis of each such 4 hour

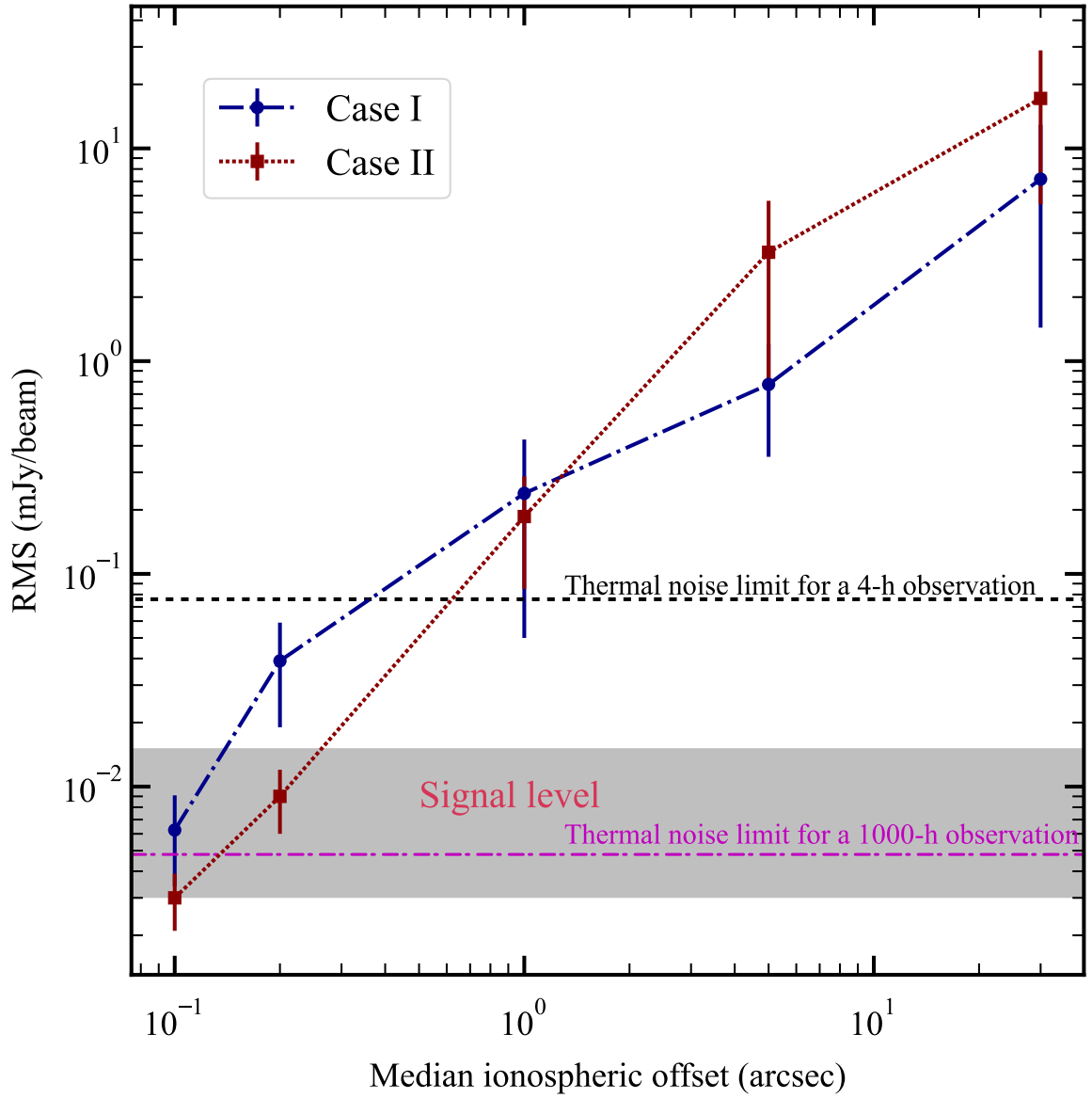


Figure 6: Variation of RMS in the residual image with ionospheric error using T-RECS as foreground model for different ionospheric frameworks considered. The RMS noise levels are plotted against the median ionospheric offset, expressed in arcseconds. The dash-dotted blue line and dotted red line showcase the RMS noise variation in Cases I and II, respectively. The dashed black line and the magenta dashed line represent the theoretical thermal noise limit for a 4 h and a 1000 h observation time. The grey band represent the H_i 21 cm signal amplitude observed by the SKA1-Low.

observation chunk, then the total thermal noise scales down as $\propto 1/\sqrt{N_{\text{days}}}$, where N_{days} is the number of days of observation. If we assume the RMS noise is limited by only thermal noise, then the RMS noise scales down to the limit of 1000 hours of observation. Hence, higher ionospheric corruptions $0.2'' \lesssim \theta_{\text{MIO}} \lesssim 1''$ will allow us to reach the final level of RMS noise to detect the 21 cm signal in the image domain. A future study will explore the presence and impact of thermal noise in the extraction of the EoR signal in the image domain in greater detail.

This work investigated how the activity levels of the ionosphere, from active to quiet conditions, affect the extraction of the target signal on the SKA1-Low observation using two different frameworks. A static phase gradient solely shifts source positions without affecting their fluxes. In contrast, time-evolving Kolmogorov-like turbulence introduces time-varying refraction at each observation step. A diffraction effect arises when imaging the combined data from the entire observation period. This effect modifies the fluxes in neighbouring pixels surrounding each source. To enhance the dynamic range and reconstruct a tomographic image of the H_I 21 cm signal, a direction-dependent calibration technique is necessary.

4 PS estimation

In this section, we outline the method for PS estimation using delay-domain formalization. The results obtained for the different ionospheric frameworks are described in the subsequent section.

4.1 Analysis method

The major aim of a CD/EoR telescope is to detect the PS of a cosmological H_I 21 cm signal. PS is the estimation of the statistical fluctuation of the H_I signal from CD/EoR. The PS can be estimated either directly from the image cube [for more, see 14, 24] or from the observed visibilities [for more details, see 26, 34, 52]; this work employs visibility for its determination. The inverse Fourier transform of $V(\mathbf{u}, \nu)$ along the frequency axis gives visibility in the delay domain, which is defined as

$$V(\mathbf{u}, \eta) = \int_{\text{sky}} V(\mathbf{u}, \nu) W(\nu) e^{2\pi i \nu \eta} d\nu \quad (4.1)$$

where η is the time delay and $W(\nu)$ is the window function given by the instrumental FoV and bandwidth. The cylindrical-averaged 2D PS [22, 75] is given by

$$P(k_{\perp}, k_{\parallel}) = \left(\frac{\lambda^2}{2k_B} \right)^2 \left(\frac{A_{\text{eff}}}{\lambda^2 B} \right) \left(\frac{D^2 \Delta D}{B} \right) |V(\mathbf{u}, \eta)|^2 \quad (4.2)$$

In equation 4.2, λ is the wavelength corresponding to the central frequency of the observation, k_B is the Boltzmann constant, B is the bandwidth, $D(z)$ is the transverse co-moving distance and $\Delta D(z)$ is the co-moving depth along the line of sight [22, 75] and A_{eff} is the effective collecting area. The wavenumbers k_{\perp} correspond to the sky plane, which is determined by the antenna baseline, and k_{\parallel} represents the line of sight of the sky, which is determined by the

spectral resolution. Longer baselines enable the probing of finer angular scales accessible on the sky, corresponding to the largest k_{\perp} modes. The spectral resolution of the interferometer limits the maximum accessible k_{\parallel} modes, while the total bandwidth constrains the minimum accessible k_{\parallel} modes [76]. The two-component of the k vector is given below,

$$k_{\perp} = \frac{2\pi|\mathbf{u}|}{D(z)} \quad (4.3)$$

$$k_{\parallel} = \frac{2\pi\eta\nu_{\text{rest}}H_0E(z)}{c(1+z)^2} \quad (4.4)$$

where ν_{rest} is the rest-frame frequency of the 21 cm spin-flip transition of HI, z is the observed redshift, H_0 is the Hubble parameter, and $E(z) \equiv [\Omega_{\text{M}}(1+z)^3 + \Omega_{\Lambda}]^{1/2}$. Ω_{M} and Ω_{Λ} are the matter and dark energy density, respectively, at the present time. The advantage of cylindrical-averaged PS is that it splits the chromatic response of the instrument. The 1D PS is obtained by the spherical averaging of $P(k_{\perp}, k_{\parallel})$ in independent k -bins, and the dimensionless 1D PS can be written as

$$\Delta^2(k) = \frac{k^3}{2\pi^2}P(k) \quad (4.5)$$

where $k = \sqrt{k_{\perp}^2 + k_{\parallel}^2}$. To determine the uncertainty in the PS estimation, we added thermal noise to the uncertainty estimation. The noise power spectrum arising from thermal noise contribution in the radio interferometric observation is given by ⁵

$$P_N^{\text{HI}} = \frac{2T_{\text{sys}}^2}{Bt_{\text{obs}}} \frac{D^2(z)\Delta D\Omega_{\text{FoV}}}{n_p} \left(\frac{A_{\text{eff}}A_{\text{core}}}{A_{\text{coll}}^2} \right) \quad (4.6)$$

where A_{core} is the core area of the array, A_{coll} is the total collection area of the array, t_{obs} is the total observation hours. We consider the PS uncertainty of the order of 3σ in a particular k -mode. It still needs to be decided with SKA1-Low if foreground removal, avoidance, or the hybrid method is used to estimate the signal PS. The spherically averaged PS was calculated in this work using the general technique of averaging across all k -modes. We consider 1000 h of observational time to calculate the uncertainty in noise PS.

4.2 Systematics effect on PS estimation

4.2.1 Case I

Figure 7 presents the PS of residual visibilities for Case I (refer to Section 4.1 for details). The left panel shows the cylindrical averaged PS for MIOs of 0.1'', 0.2'', 1'' and 5''. The solid black line represents the horizon limit. Spectrally smooth foreground interference with ionospheric contamination spills over power beyond the wedge-shaped region in 2D space. Point sources are located at the largest k_{\perp} scales. Imperfect gain calibration leads to residual point sources spilling over power beyond the wedge and into the EoR window in the frequency

⁵This equation is the modified form employed in the literature [77]

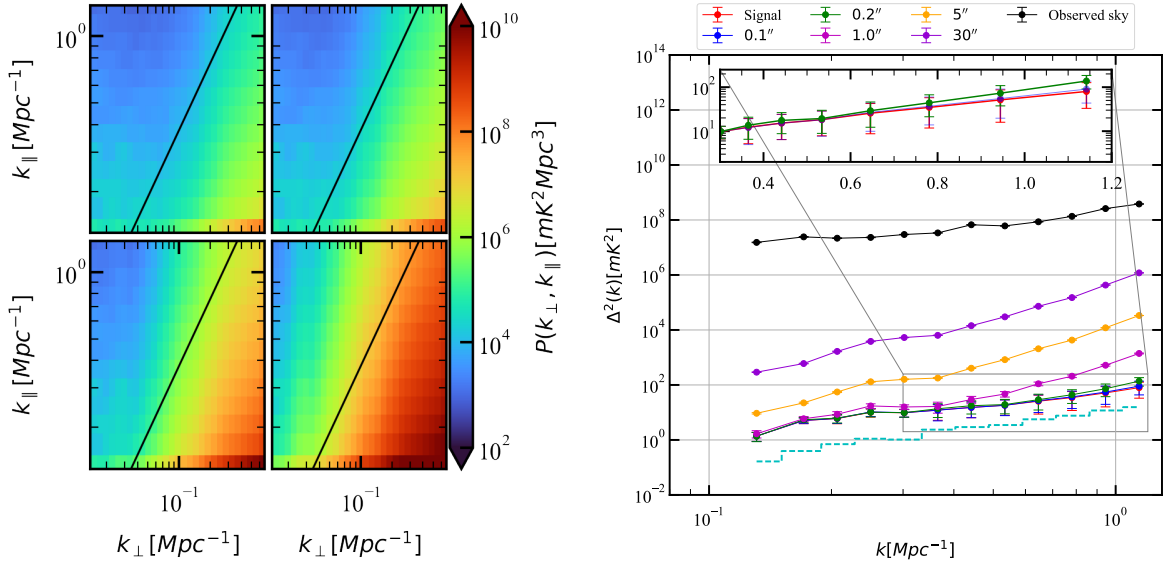


Figure 7: Left: Residual PS depicting ionospheric errors associated with SKA1-Low for Case I. Cylindrical averaged power spectra for residual visibilities for ionospheric errors with MIOs of $0.1''$ (top left), $0.2''$ (top right), $1''$ (bottom left) and $5''$ (bottom right). The solid black line represents the horizon line. **Right:** Comparison of the spherical averaged PS showing ionospheric errors with the signal and residual foreground power. The error bars are the total uncertainties of 3σ sample variance and thermal noise for all k -modes. The cyan line represents the total sensitivity limit of sample variance and 1000 h of observation of instrumental noise.

scales [78]. This contamination becomes more severe when the apparent shift of the sources from the origin increases, signifies active ionospheric activity. This simulation aims to determine how turbulence level leaks the power into the EoR window without considering the direction-dependent calibration effect. As expected, the higher ionospheric turbulence level results in greater contamination within the EoR window. The right panel of Figure 7 displays the spherical averaged PS of residual visibilities. The solid red and black line represents the H_I 21 cm signal PS and the observed sky PS (foreground plus H_I 21 cm signal) as measured by SKA1-Low. The inset highlights the area near the signal power for k -modes greater than 0.2 Mpc^{-1} . The residual PS overlaps with the signal power within the error bars as long as the apparent source position shift remains below $\sim 0.2''$. Therefore, the MIO of $0.2''$, for this case, represents the tolerable limit for accurately measuring the signal PS. At the MIO of $1.0''$, the residual amplitude becomes significantly high for all k -modes, indicating severe bias in the estimated cosmological PS due to residual foreground contamination.

4.2.2 Case II

The ionospheric contamination for this case of the delay power spectrum is demonstrated in Figure 8, for different ionospheric activity with MIOs of $0.1''$, $0.2''$, $1''$ and $5''$. It is observed that the residual power leakage significantly affects the EoR window from the wedge more

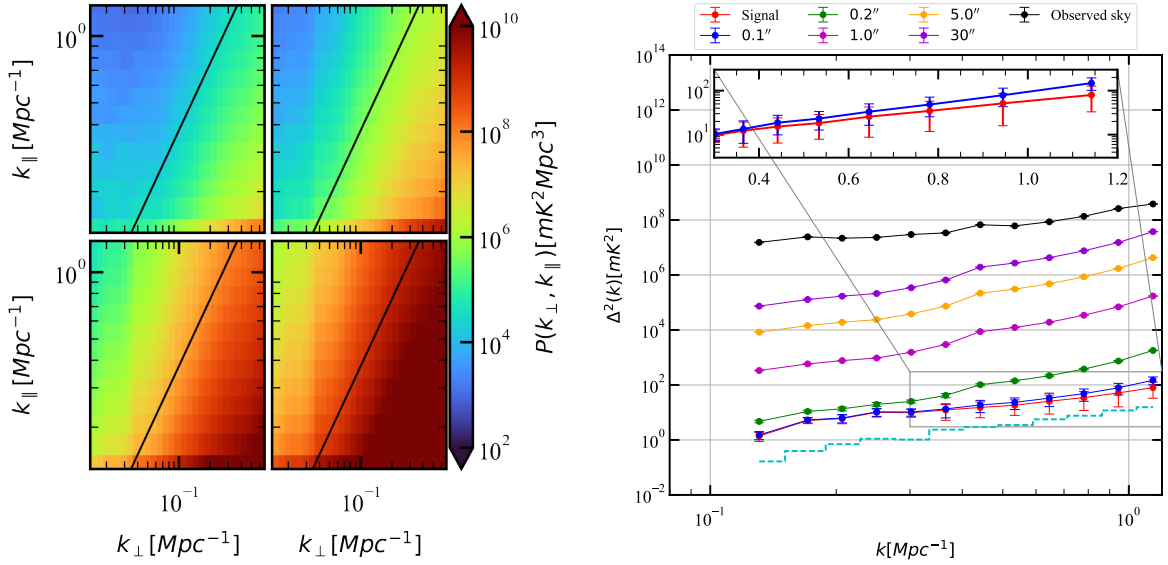


Figure 8: **Left:** Residual PS depicting ionospheric errors associated with SKA1-Low for Case II. Cylindrical averaged power spectra for residual visibilities for ionospheric errors with MIOs of $0.1''$ (top-left), $0.2''$ (top-right), $1''$ (bottom-left), $5''$ (bottom-right). The solid black line represents the horizon line. **Right:** Comparison of the spherical averaged PS showing ionospheric errors with the signal and residual foreground power. The error bars are the total uncertainties of 3σ sample variance and thermal noise for all k -modes. The cyan line represents the total sensitivity limit of sample variance and 1000 hours of observation of instrumental noise.

than in case I as we increase the activity level from quiet to extremely active condition. As we continue with this figure, the right panel shows the spherical averaged PS using all the accessible k -modes. We observe that the residual PS tracks the signal PS for the MIO value of $0.1''$. Therefore, this MIO represents the tolerance level for precision measurements of the signal PS. Beyond this MIO of $0.1''$, the residual power surpasses the target signal PS across all accessible k -modes, potentially leading to biased estimations of the cosmological PS.

Our findings indicate that for $\theta_{\text{MIO}} \lesssim 0.1''$, the 21 cm signal originating from the EoR surpasses any remaining calibration inaccuracies caused by the Earth’s ionosphere. This initial systematic investigation highlights the importance of implementing ionospheric calibration for the forthcoming SKA1-Low observations. It further emphasizes the necessity of investigating the potential impact of any residual gain errors on the final H_I 21 cm PS.

5 Summary and conclusions

In this work, we have extended the end-to-end (21CME2E) pipeline described in [34] to include additional effects on the recovery of the PS of the H_I 21 cm signal from the EoR. This target signal has most of its power concentrated at small k -scales (or large spatial scales). Thus, for an EoR experiment with an interferometric array, short baselines dictate

most of the sensitivity. We use the extended pipeline to evaluate the effects of the Earth’s ionosphere on target signal recovery in both the image and the power spectrum domains. We used two different frameworks to understand the effect of time-varying ionospheric activity on the synthetic CD/EoR observations with the compact core of SKA1-Low. We consider the dynamic ionosphere updates every 2 minute cadence with a period of 4 hours of observation. However, real-world ionospheric conditions can vary significantly within short timescales, in less than 10 seconds, as demonstrated in [79, 80]. We present the results obtained through synthetic observations using different ionospheric frameworks. The results can be summarized as follows:

1. Our simulations revealed that different frameworks of ionospheric corruption, including simple phase shifts and turbulence-induced effects, have distinct impacts on the detectability of the target EoR signal. Our analysis suggests that a tolerance level of $0.2'' \lesssim \theta_{\text{MIO}} \lesssim 1''$ is necessary to extract the EoR signal in the image domain in the presence of ionospheric corruption. However, this tolerance level should be adapted to account for the variations in RMS noise across different sky fields. When the MIO exceeds this threshold value, residual foreground contamination can significantly hinder the detection of the EoR signal by obscuring it. The required optimum astrometric accuracy ($0.2'' \lesssim \theta_{\text{MIO}} \lesssim 1''$) is achievable with upcoming SKA1-Low observations. For example, the LOFAR Two-metre Sky Survey (LoTSS) achieved a position accuracy of $\sim 0.2''$ between 120 and 168 MHz ([81]). The GLEAM survey achieved an accuracy better than $\sim 2''$ between 70 and 231 MHz ([82, 83]). With its improved sensitivity, SKA1-Low is expected to generate sufficiently accurate sky models for making tomographic maps of the EoR.
2. At the MRO location, previous studies [12, 45, 46, 52, 53, 84] have characterized and assessed the impact of ionospheric corruption on the PS estimation. We quantify the level of ionospheric corruption tolerable for precision PS estimation. Our results demonstrate that the recoverable PS of the H_I signal surpasses any remaining calibration inaccuracies caused by the Earth’s ionosphere depending on the dominant mode of ionospheric corruption. In the case of time-varying phase offsets, with $\theta_{\text{MIO}} \sim 0.2''$, the EoR signal remains detectable. However, under the most realistic turbulent conditions modelled by Kolmogorov statistics, residual power becomes excessively high beyond an offset of $\theta_{\text{MIO}} \lesssim 0.1''$, thereby hindering H_I 21 cm signal extraction. The tolerance levels presented here are based on the compact core of SKA1-Low. The impact of ionospheric corruption on longer baselines dictates further investigation and will be a subject of future research. In summary, these results indicate that understanding the ionospheric conditions during observation runs for EoR science is essential because such unaccounted effects, even to the first order, can adversely affect signal extraction.

In this work, we have presented the effects of the Earth’s ionosphere, one of the most difficult to resolve issues at low frequencies, on sensitive radio observations. It is to be noted that our current analysis does not account for factors like diffuse foreground emission, thermal noise, and the impact of longer baselines on the observed data. We also assume that other effects like direction-independent gain errors are perfectly accounted for. These omitted

complexities further challenge the quantification of ionospheric effects and its overall impact on real data. These considerations are deferred to future studies. We are incorporating further features into the end-to-end pipeline to study more complex systematic effects and test different methods (like Largest Cluster Statistics) to improve extraction of the reionization history from observed data in the presence of the real imperfections expected to be present in the SKA1-Low data.

Acknowledgments

SKP acknowledges the financial support by the Department of Science and Technology, Government of India, through the INSPIRE Fellowship. AM thanks the UK Research and Innovation Future Leaders Fellowship for supporting this research [grant MR/V026437/1]. The authors thank the anonymous reviewer and scientific editor for their insightful comments and suggestions, which significantly improved the quality of this manuscript.

Software: This work is heavily based on the Python programming language (<https://www.python.org/>). The packages used here are `astropy` (<https://www.astropy.org/>, [85, 86]), `numpy` (<https://numpy.org/>), `h5py` (<https://www.h5py.org/>), `matplotlib` (<https://matplotlib.org/>), `seaborn` (<https://seaborn.pydata.org/>), `scipy` (<https://scipy.org/>), `pyuvdata` (<https://github.com/RadioAstronomySoftwareGroup>), `OSKAR` has been used for simulations (<https://github.com/OxfordSKA/OSKAR>), and Common Astronomy Software Applications (CASA) (<https://casa.nrao.edu/casadocs>) are used for imaging.

Appendix

To test the ionospheric effect on visibility simulations conducted with `OSKAR`, we inserted a two-dimensional phase screen between the source and the array. This screen represents a simplified ionosphere with a constant phase gradient across the field of view in one direction. In a compact array configuration, all antennas observe this same ionospheric condition. This constant phase gradient primarily affects the angular position shift of cosmic sources without change distorting the shape of the source. Importantly, Earth aperture synthesis relies on the movement of baseline projections with observation time, effectively filling the u - v plane. Consequently, a static spatial phase gradient transforms into a time-varying gradient in the u - v domain. When we form a synthesized image from a single snapshot observation, this results in source extension and variable amplitude. The phase screen values correspond to a ΔTEC above the station. The `OSKAR` package⁶ then converts these values into phase shifts and applies them to each source and array element. Figure 9 shows the constant gradient ionospheric structure.

⁶<https://ska-telescope.gitlab.io/sim/oskar/theory/theory.html>

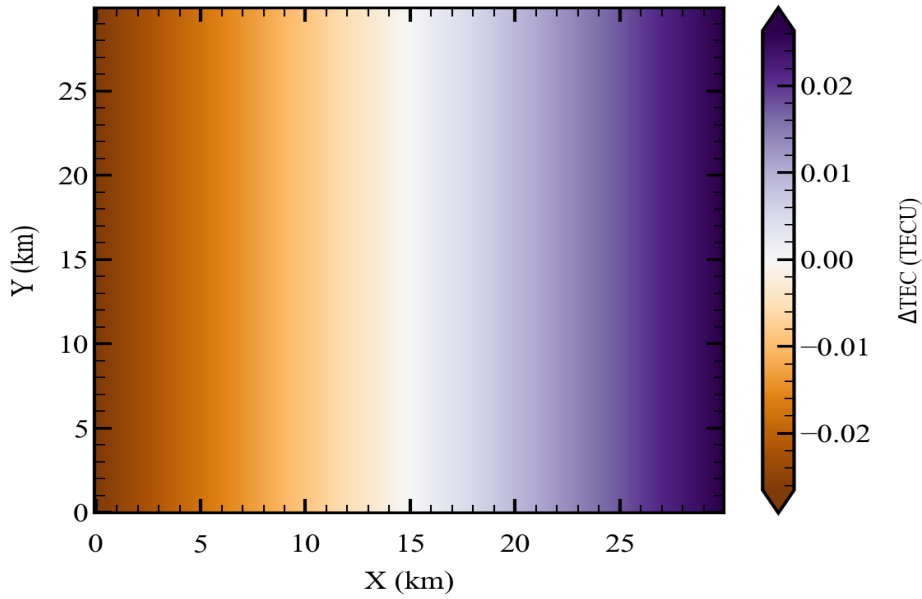


Figure 9: The two-dimensional phase-screen model has a constant gradient and dimension size of 30 km on each side, with 300×300 grid size. At the 400 km altitude, the ionospheric screen covered the sources within the field of view.

References

- [1] E. Komatsu, K.M. Smith, J. Dunkley, C.L. Bennett, B. Gold, G. Hinshaw et al., *Seven-year Wilkinson Microwave Anisotropy Probe (WMAP) Observations: Cosmological Interpretation*, *Astrophys. J. Suppl.* **192** (2011) 18 [[1001.4538](#)].
- [2] Planck Collaboration, N. Aghanim, Y. Akrami, F. Arroja, M. Ashdown, J. Aumont et al., *Planck 2018 results. I. Overview and the cosmological legacy of Planck*, *Astron. Astrophys.* **641** (2020) A1 [[1807.06205](#)].
- [3] M. Ouchi, K. Shimasaku, H. Furusawa, T. Saito, M. Yoshida, M. Akiyama et al., *Statistics of 207 Ly α Emitters at a Redshift Near 7: Constraints on Reionization and Galaxy Formation Models*, *Astrophys. J.* **723** (2010) 869 [[1007.2961](#)].
- [4] K. Ota, M. Iye, N. Kashikawa, A. Konno, F. Nakata, T. Totani et al., *A New Constraint on Reionization from the Evolution of the Ly α Luminosity Function at $z \sim 6-7$ Probed by a Deep Census of $z = 7.0$ Ly α Emitter Candidates to $0.3L^*$* , *Astrophys. J.* **844** (2017) 85 [[1703.02501](#)].
- [5] X. Fan, M.A. Strauss, D.P. Schneider, R.H. Becker, R.L. White, Z. Haiman et al., *A Survey of $z > 5.7$ Quasars in the Sloan Digital Sky Survey. II. Discovery of Three Additional Quasars at $z > 6$* , *Astron. J.* **125** (2003) 1649 [[astro-ph/0301135](#)].
- [6] T. Goto, Y. Utsumi, J.R. Walsh, T. Hattori, S. Miyazaki and C. Yamauchi, *Spectroscopy of the spatially extended Ly α emission around a quasar at $z = 6.4$* , *Mon. Not. Roy. Astron. Soc.* **421** (2012) L77 [[1112.3656](#)].
- [7] R. Barnett, S.J. Warren, G.D. Becker, D.J. Mortlock, P.C. Hewett, R.G. McMahon et al.,

- Observations of the Lyman series forest towards the redshift 7.1 quasar ULAS J1120+0641*, *Astron. Astrophys.* **601** (2017) A16 [[1702.03687](#)].
- [8] S.R. Furlanetto, S.P. Oh and F.H. Briggs, *Cosmology at low frequencies: The 21 cm transition and the high-redshift Universe*, *Physics Reports* **433** (2006) 181 [[astro-ph/0608032](#)].
- [9] T.R. Choudhury, M.G. Haehnelt and J. Regan, *Inside-out or outside-in: the topology of reionization in the photon-starved regime suggested by Ly α forest data*, *Mon. Not. Roy. Astron. Soc.* **394** (2009) 960 [[0806.1524](#)].
- [10] J.R. Pritchard and A. Loeb, *21 cm cosmology in the 21st century*, *Reports on Progress in Physics* **75** (2012) 086901 [[1109.6012](#)].
- [11] N. Barry, M. Wilensky, C.M. Trott, B. Pindor, A.P. Beardsley, B.J. Hazelton et al., *Improving the Epoch of Reionization Power Spectrum Results from Murchison Widefield Array Season 1 Observations*, *Astrophys. J.* **884** (2019) 1 [[1909.00561](#)].
- [12] S. Yoshiura, B. Pindor, J.L.B. Line, N. Barry, C.M. Trott, A. Beardsley et al., *A new MWA limit on the 21 cm power spectrum at redshifts 13-17*, *Mon. Not. Roy. Astron. Soc.* **505** (2021) 4775 [[2105.12888](#)].
- [13] M. Kolopanis, J.C. Pober, D.C. Jacobs and S. McGraw, *New EoR power spectrum limits from MWA Phase II using the delay spectrum method and novel systematic rejection*, *Mon. Not. Roy. Astron. Soc.* **521** (2023) 5120 [[2210.10885](#)].
- [14] F.G. Mertens, M. Mevius, L.V.E. Koopmans, A.R. Offringa, G. Mellema, S. Zaroubi et al., *Improved upper limits on the 21 cm signal power spectrum of neutral hydrogen at $z \approx 9.1$ from LOFAR*, *Mon. Not. Roy. Astron. Soc.* **493** (2020) 1662 [[2002.07196](#)].
- [15] G. Paciga, J.G. Albert, K. Bandura, T.-C. Chang, Y. Gupta, C. Hirata et al., *A simulation-calibrated limit on the HI power spectrum from the GMRT Epoch of Reionization experiment*, *Mon. Not. Roy. Astron. Soc.* **433** (2013) 639 [[1301.5906](#)].
- [16] M. Kolopanis, D.C. Jacobs, C. Cheng, A.R. Parsons, S.A. Kohn, J.C. Pober et al., *A Simplified, Lossless Reanalysis of PAPER-64*, *Astrophys. J.* **883** (2019) 133 [[1909.02085](#)].
- [17] D.R. DeBoer, A.R. Parsons, J.E. Aguirre, P. Alexander, Z.S. Ali, A.P. Beardsley et al., *Hydrogen Epoch of Reionization Array (HERA)*, *Publ. Astron. Soc. Pac* **129** (2017) 045001 [[1606.07473](#)].
- [18] Z. The HERA Collaboration, J.E. Aguirre, P. Alexander, Z.S. Ali, Y. Balfour, A.P. Beardsley et al., *First Results from HERA Phase I: Upper Limits on the Epoch of Reionization 21 cm Power Spectrum*, *Astrophys. J.* **925** (2022) 221 [[2108.02263](#)].
- [19] HERA Collaboration, Z. Abdurashidova, T. Adams, J.E. Aguirre, P. Alexander, Z.S. Ali et al., *Improved Constraints on the 21 cm EoR Power Spectrum and the X-Ray Heating of the IGM with HERA Phase I Observations*, *Astrophys. J.* **945** (2023) 124.
- [20] A. Datta, J.D. Bowman and C.L. Carilli, *Bright Source Subtraction Requirements for Redshifted 21 cm Measurements*, *Astrophys. J.* **724** (2010) 526 [[1005.4071](#)].
- [21] H. Vedantham, N. Udaya Shankar and R. Subrahmanyam, *Imaging the Epoch of Reionization: Limitations from Foreground Confusion and Imaging Algorithms*, *Astrophys. J.* **745** (2012) 176 [[1106.1297](#)].

- [22] N. Thyagarajan, D.C. Jacobs, J.D. Bowman, N. Barry, A.P. Beardsley, G. Bernardi et al., *Foregrounds in Wide-field Redshifted 21 cm Power Spectra*, *Astrophys. J.* **804** (2015) 14 [[1502.07596](#)].
- [23] N. Thyagarajan, D.C. Jacobs, J.D. Bowman, N. Barry, A.P. Beardsley, G. Bernardi et al., *Confirmation of Wide-field Signatures in Redshifted 21 cm Power Spectra*, *Astrophys. J.* **807** (2015) L28 [[1506.06150](#)].
- [24] F.G. Mertens, A. Ghosh and L.V.E. Koopmans, *Statistical 21-cm signal separation via Gaussian Process Regression analysis*, *Mon. Not. Roy. Astron. Soc.* **478** (2018) 3640 [[1711.10834](#)].
- [25] I. Hothi, E. Chapman, J.R. Pritchard, F.G. Mertens, L.V.E. Koopmans, B. Ciardi et al., *Comparing foreground removal techniques for recovery of the LOFAR-EoR 21 cm power spectrum*, *Mon. Not. Roy. Astron. Soc.* **500** (2021) 2264 [[2011.01284](#)].
- [26] N.S. Kern and A. Liu, *Gaussian process foreground subtraction and power spectrum estimation for 21 cm cosmology*, *Mon. Not. Roy. Astron. Soc.* **501** (2021) 1463 [[2010.15892](#)].
- [27] A.R. Offringa, R.B. Wayth, N. Hurley-Walker, D.L. Kaplan, N. Barry, A.P. Beardsley et al., *The Low-Frequency Environment of the Murchison Widefield Array: Radio-Frequency Interference Analysis and Mitigation*, *Publ. Astron. Soc. Austral.* **32** (2015) e008 [[1501.03946](#)].
- [28] N. Barry, B. Hazelton, I. Sullivan, M.F. Morales and J.C. Pober, *Calibration requirements for detecting the 21 cm epoch of reionization power spectrum and implications for the SKA*, *Mon. Not. Roy. Astron. Soc.* **461** (2016) 3135 [[1603.00607](#)].
- [29] C.M. Trott and R.B. Wayth, *Spectral Calibration Requirements of Radio Interferometers for Epoch of Reionisation Science with the SKA*, *Publ. Astron. Soc. Austral.* **33** (2016) e019 [[1604.03273](#)].
- [30] A. Ewall-Wice, J.S. Dillon, A. Liu and J. Hewitt, *The impact of modelling errors on interferometer calibration for 21 cm power spectra*, *Mon. Not. Roy. Astron. Soc.* **470** (2017) 1849 [[1610.02689](#)].
- [31] A.H. Patil, S. Yatawatta, L.V.E. Koopmans, A.G. de Bruyn, M.A. Brentjens, S. Zaroubi et al., *Upper Limits on the 21 cm Epoch of Reionization Power Spectrum from One Night with LOFAR*, *Astrophys. J.* **838** (2017) 65 [[1702.08679](#)].
- [32] J.S. Dillon, S.A. Kohn, A.R. Parsons, J.E. Aguirre, Z.S. Ali, G. Bernardi et al., *Polarized redundant-baseline calibration for 21 cm cosmology without adding spectral structure*, *Mon. Not. Roy. Astron. Soc.* **477** (2018) 5670 [[1712.07212](#)].
- [33] N.S. Kern, A.R. Parsons, J.S. Dillon, A.E. Lanman, N. Fagnoni and E. de Lera Acedo, *Mitigating Internal Instrument Coupling for 21 cm Cosmology. I. Temporal and Spectral Modeling in Simulations*, *Astrophys. J.* **884** (2019) 105.
- [34] A. Mazumder, A. Datta, A. Chakraborty and S. Majumdar, *Observing the reionization: effect of calibration and position errors on realistic observation conditions*, *Mon. Not. Roy. Astron. Soc.* **515** (2022) 4020 [[2207.06169](#)].
- [35] E. de Lera Acedo, C.M. Trott, R.B. Wayth, N. Fagnoni, G. Bernardi, B. Wakley et al., *Spectral performance of SKA Log-periodic Antennas I: mitigating spectral artefacts in SKA1-LOW 21 cm cosmology experiments*, *Mon. Not. Roy. Astron. Soc.* **469** (2017) 2662 [[1702.05126](#)].

- [36] C.M. Trott, E. de Lera Acedo, R.B. Wayth, N. Fagnoni, A.T. Sutinjo, B. Wakley et al., *Spectral performance of Square Kilometre Array Antennas - II. Calibration performance*, *Mon. Not. Roy. Astron. Soc.* **470** (2017) 455 [[1705.03116](#)].
- [37] R.C. Joseph, C.M. Trott and R.B. Wayth, *The Bias and Uncertainty of Redundant and Sky-based Calibration Under Realistic Sky and Telescope Conditions*, *Astron. J.* **156** (2018) 285 [[1810.11237](#)].
- [38] W. Li, J.C. Pober, B.J. Hazelton, N. Barry, M.F. Morales, I. Sullivan et al., *Comparing Redundant and Sky-model-based Interferometric Calibration: A First Look with Phase II of the MWA*, *Astrophys. J.* **863** (2018) 170 [[1807.05312](#)].
- [39] A.R. Parsons, D.C. Backer, G.S. Foster, M.C.H. Wright, R.F. Bradley, N.E. Gugliucci et al., *The Precision Array for Probing the Epoch of Re-ionization: Eight Station Results*, *Astron. J.* **139** (2010) 1468 [[0904.2334](#)].
- [40] A. Parsons, J. Pober, M. McQuinn, D. Jacobs and J. Aguirre, *A Sensitivity and Array-configuration Study for Measuring the Power Spectrum of 21 cm Emission from Reionization*, *Astrophys. J.* **753** (2012) 81 [[1103.2135](#)].
- [41] S. Choudhuri, S. Bharadwaj, A. Ghosh and S.S. Ali, *Visibility-based angular power spectrum estimation in low-frequency radio interferometric observations*, *Mon. Not. Roy. Astron. Soc.* **445** (2014) 4351 [[1409.7789](#)].
- [42] A. Liu, A.R. Parsons and C.M. Trott, *Epoch of reionization window. I. Mathematical formalism*, *Phys. Rev.* **90** (2014) 023018 [[1404.2596](#)].
- [43] S. Choudhuri, S. Bharadwaj, S. Chatterjee, S.S. Ali, N. Roy and A. Ghosh, *The visibility-based tapered gridded estimator (TGE) for the redshifted 21-cm power spectrum*, *Mon. Not. Roy. Astron. Soc.* **463** (2016) 4093 [[1609.01732](#)].
- [44] A.R. Offringa, F. Mertens, S. van der Tol, B. Veenboer, B.K. Gehlot, L.V.E. Koopmans et al., *Precision requirements for interferometric gridding in the analysis of a 21 cm power spectrum*, *Astron. Astrophys.* **631** (2019) A12 [[1908.11232](#)].
- [45] C.H. Jordan, S. Murray, C.M. Trott, R.B. Wayth, D.A. Mitchell, M. Rahimi et al., *Characterization of the ionosphere above the Murchison Radio Observatory using the Murchison Widefield Array*, *Mon. Not. Roy. Astron. Soc.* **471** (2017) 3974 [[1707.04978](#)].
- [46] C.M. Trott, C.H. Jordan, S.G. Murray, B. Pindor, D.A. Mitchell, R.B. Wayth et al., *Assessment of Ionospheric Activity Tolerances for Epoch of Reionization Science with the Murchison Widefield Array*, *Astrophys. J.* **867** (2018) 15.
- [47] J.F. Helmboldt and N. Hurley-Walker, *Ionospheric Irregularities Observed During the GLEAM Survey*, *Radio Science* **55** (2020) e07106.
- [48] M.J. Wilensky, M.F. Morales, B.J. Hazelton, N. Barry, R. Byrne and S. Roy, *Absolving the SSINS of Precision Interferometric Radio Data: A New Technique for Mitigating Faint Radio Frequency Interference*, *Publ. Astron. Soc. Pac* **131** (2019) 114507 [[1906.01093](#)].
- [49] M. Sokolowski, T. Colegate, A.T. Sutinjo, D. Ung, R. Wayth, N. Hurley-Walker et al., *Calibration and Stokes Imaging with Full Embedded Element Primary Beam Model for the Murchison Widefield Array*, *Publ. Astron. Soc. Austral.* **34** (2017) e062 [[1710.07478](#)].
- [50] A. Nasirudin, D. Prelogovic, S.G. Murray, A. Mesinger and G. Bernardi, *Characterizing beam*

errors for radio interferometric observations of reionization, *Mon. Not. Roy. Astron. Soc.* **514** (2022) 4655 [2201.10798].

- [51] C.J. Lonsdale, *Radio astronomy at long wavelengths with the Murchison widefield array*, in *From Clark Lake to the Long Wavelength Array: Bill Erickson's Radio Science*, N. Kassim, M. Perez, W. Junor and P. Henning, eds., vol. 345 of *Astronomical Society of the Pacific Conference Series*, p. 399, 2005.
- [52] C.M. Trott, C.H. Jordan, S. Midgley, N. Barry, B. Greig, B. Pindor et al., *Deep multiredshift limits on Epoch of Reionization 21 cm power spectra from four seasons of Murchison Widefield Array observations*, *Mon. Not. Roy. Astron. Soc.* **493** (2020) 4711 [2002.02575].
- [53] A.P. Beardsley, B.J. Hazelton, I.S. Sullivan, P. Carroll, N. Barry, M. Rahimi et al., *First Season MWA EoR Power spectrum Results at Redshift 7*, *Astrophys. J.* **833** (2016) 102 [1608.06281].
- [54] A. Ewall-Wice, J.S. Dillon, J.N. Hewitt, A. Loeb, A. Mesinger, A.R. Neben et al., *First limits on the 21 cm power spectrum during the Epoch of X-ray heating*, *Mon. Not. Roy. Astron. Soc.* **460** (2016) 4320 [1605.00016].
- [55] H. Gan, F.G. Mertens, L.V.E. Koopmans, A.R. Offringa, M. Mevius, V.N. Pandey et al., *Assessing the impact of two independent direction-dependent calibration algorithms on the LOFAR 21 cm signal power spectrum. And applications to an observation of a field flanking the north celestial pole*, *Astron. Astrophys.* **669** (2023) A20.
- [56] J.P. McMullin, B. Waters, D. Schiebel, W. Young and K. Golap, *CASA Architecture and Applications*, in *Astronomical Data Analysis Software and Systems XVI*, R.A. Shaw, F. Hill and D.J. Bell, eds., vol. 376 of *Astronomical Society of the Pacific Conference Series*, p. 127, October, 2007.
- [57] J.P. Hamaker, J.D. Bregman and R.J. Sault, *Understanding radio polarimetry. I. Mathematical foundations.*, *Astronomy and Astrophysics Supplement Series* **117** (1996) 137.
- [58] A. Mesinger, S. Furlanetto and R. Cen, *21CMFAST: a fast, seminumerical simulation of the high-redshift 21-cm signal*, *Mon. Not. Roy. Astron. Soc.* **411** (2011) 955 [1003.3878].
- [59] S. Murray, B. Greig, A. Mesinger, J. Muñoz, Y. Qin, J. Park et al., *21cmFAST v3: A Python-integrated C code for generating 3D realizations of the cosmic 21cm signal.*, *The Journal of Open Source Software* **5** (2020) 2582 [2010.15121].
- [60] A. Bonaldi, M. Bonato, V. Galluzzi, I. Harrison, M. Massardi, S. Kay et al., *The Tiered Radio Extragalactic Continuum Simulation (T-RECS)*, *Mon. Not. Roy. Astron. Soc.* **482** (2019) 2 [1805.05222].
- [61] P. Dewdney and R. Braun, *Ska1-low configuration coordinates –complete set*, May, 2016.
- [62] R.B. Wayth, E. Lenc, M.E. Bell, J.R. Callingham, K.S. Dwarakanath, T.M.O. Franzen et al., *GLEAM: The GaLactic and Extragalactic All-Sky MWA Survey*, *Publ. Astron. Soc. Austral.* **32** (2015) e025 [1505.06041].
- [63] J.A. Ratcliffe, *Some Aspects of Diffraction Theory and their Application to the Ionosphere*, *Reports on Progress in Physics* **19** (1956) 188.
- [64] H.T. Intema, S. van der Tol, W.D. Cotton, A.S. Cohen, I.M. van Bemmelen and H.J.A. Röttgering, *Ionospheric calibration of low frequency radio interferometric observations using the peeling scheme. I. Method description and first results*, *Astron. Astrophys.* **501** (2009) 1185 [0904.3975].

- [65] M. Mevius, S. van der Tol, V.N. Pandey, H.K. Vedantham, M.A. Brentjens, A.G. de Bruyn et al., *Probing ionospheric structures using the LOFAR radio telescope*, *Radio Science* **51** (2016) 927 [[1606.04683](#)].
- [66] R.L. A. Glindemann and J. Dainty, *Simulation of time-evolving speckle patterns using kolmogorov statistics*, *Journal of Modern Optics* **40** (1993) 2381 [<https://doi.org/10.1080/09500349314552401>].
- [67] B.G. Fejer and M.C. Kelley, *Ionospheric irregularities.*, *Reviews of Geophysics and Space Physics* **18** (1980) 401.
- [68] P.J. Hancock, C.M. Trott and N. Hurley-Walker, *Source Finding in the Era of the SKA (Precursors): Aegean 2.0*, *Publ. Astron. Soc. Austral.* **35** (2018) e011 [[1801.05548](#)].
- [69] G. Mellema, L. Koopmans, H. Shukla, K.K. Datta, A. Mesinger and S. Majumdar, *HI tomographic imaging of the Cosmic Dawn and Epoch of Reionization with SKA*, *PoS AASKA14* (2015) 010.
- [70] A. Kapahtia, P. Chingangbam, R. Ghara, S. Appleby and T.R. Choudhury, *Prospects of constraining reionization model parameters using Minkowski tensors and Betti numbers*, *JCAP* **2021** (2021) 026 [[2101.03962](#)].
- [71] S. Bag, R. Mondal, P. Sarkar, S. Bharadwaj and V. Sahni, *The shape and size distribution of H II regions near the percolation transition*, *Mon. Not. Roy. Astron. Soc.* **477** (2018) 1984 [[1801.01116](#)].
- [72] S. Dasgupta, S.K. Pal, S. Bag, S. Dutta, S. Majumdar, A. Datta et al., *Interpreting the hi 21-cm cosmology maps through largest cluster statistics. part i. impact of the synthetic ska1-low observations*, *Journal of Cosmology and Astroparticle Physics* **2023** (2023) 014.
- [73] R.A. Perley, *High Dynamic Range Imaging*, in *Synthesis Imaging in Radio Astronomy II*, G.B. Taylor, C.L. Carilli and R.A. Perley, eds., vol. 180 of *Astronomical Society of the Pacific Conference Series*, p. 275, January, 1999.
- [74] A. Datta, S. Bhatnagar and C.L. Carilli, *Detection of Signals from Cosmic Reionization Using Radio Interferometric Signal Processing*, *Astrophys. J.* **703** (2009) 1851 [[0908.2639](#)].
- [75] M.F. Morales and J. Hewitt, *Toward Epoch of Reionization Measurements with Wide-Field Radio Observations*, *Astrophys. J.* **615** (2004) 7 [[astro-ph/0312437](#)].
- [76] A. Liu and J.R. Shaw, *Data analysis for precision 21 cm cosmology*, *Publications of the Astronomical Society of the Pacific* **132** (2020) 062001.
- [77] P. Bull, P.G. Ferreira, P. Patel and M.G. Santos, *Late-time Cosmology with 21 cm Intensity Mapping Experiments*, *Astrophys. J.* **803** (2015) 21 [[1405.1452](#)].
- [78] J.D. Bowman, M.F. Morales and J.N. Hewitt, *Foreground Contamination in Interferometric Measurements of the Redshifted 21 cm Power Spectrum*, *Astrophys. J.* **695** (2009) 183 [[0807.3956](#)].
- [79] S. Mangla and A. Datta, *Study of the equatorial ionosphere using the Giant Metrewave Radio Telescope (GMRT) at sub-GHz frequencies*, *Mon. Not. Roy. Astron. Soc.* **513** (2022) 964 [[2204.04230](#)].
- [80] S. Mangla, S. Chakraborty, A. Datta and A. Paul, *Exploring Earth's ionosphere and its effect on low radio frequency observation with the uGMRT and the SKA*, *Journal of Astrophysics and Astronomy* **44** (2023) 2 [[2211.09738](#)].

- [81] T.W. Shimwell, C. Tasse, M.J. Hardcastle, A.P. Mechev, W.L. Williams, P.N. Best et al., *The LOFAR Two-metre Sky Survey. II. First data release*, *Astron. Astrophys.* **622** (2019) A1 [1811.07926].
- [82] N. Hurley-Walker, J.R. Callingham, P.J. Hancock, T.M.O. Franzen, L. Hindson, A.D. Kapińska et al., *GaLactic and Extragalactic All-sky Murchison Widefield Array (GLEAM) survey - I. A low-frequency extragalactic catalogue*, *Mon. Not. Roy. Astron. Soc.* **464** (2017) 1146 [1610.08318].
- [83] N. Hurley-Walker, P.J. Hancock, T.M.O. Franzen, J.R. Callingham, A.R. Offringa, L. Hindson et al., *GaLactic and Extragalactic All-sky Murchison Widefield Array (GLEAM) survey II: Galactic plane $345^\circ < l < 67^\circ$, $180^\circ < l < 240^\circ$* , *Publ. Astron. Soc. Austral.* **36** (2019) e047 [1911.08127].
- [84] J. Kariuki Chege, C.H. Jordan, C. Lynch, C.M. Trott, J.L.B. Line, B. Pindor et al., *Optimising MWA EoR data processing for improved 21 cm power spectrum measurements – fine-tuning ionospheric corrections*, *arXiv e-prints* (2022) arXiv:2207.12090 [2207.12090].
- [85] Astropy Collaboration, T.P. Robitaille, E.J. Tollerud, P. Greenfield, M. Droettboom, E. Bray et al., *Astropy: A community Python package for astronomy*, *Astron. Astrophys.* **558** (2013) A33 [1307.6212].
- [86] Astropy Collaboration, A.M. Price-Whelan, B.M. Sipőcz, H.M. Günther, P.L. Lim, S.M. Crawford et al., *The Astropy Project: Building an Open-science Project and Status of the v2.0 Core Package*, *Astron. J.* **156** (2018) 123 [1801.02634].